Calibration of Polarimetric Millimeter MIMO Radar for Near-Field Ultrawideband Imaging Measurement

Xiaoyu He (何晓雨)⊙, Tianjin Liu (刘天金)⊙, Jingzhe Shan (单敬喆)⊙, and Xiaojian Xu (许小剑)⊙, *Member, IEEE*

Abstract— In this article, a polarimetric multiple input multiple output (MIMO) radar with a linear antenna array including eight transmitters and 12 receivers is developed and calibrated for near-field imaging measurement in frequency band spanning from 26.5 to 38 GHz. In the system hardware configuration, the single-polarized antennas are connected to a vector network analyzer (VNA) through a radio frequency (RF) switch matrix as a compromise of performance and expense. A two-step system calibration procedure is proposed in the compensation of signal distortion, where the measured polarimetric data of specified calibrators is compared with the simulation results at each channel to solve the compensation coefficients for frequency response. The measured 2-D radar images are generated by means of back projection (BP), in which the weight coefficient of each channel is calculated to minimize the difference in the simulation counterparts. The full polarimetric data of vehicles is acquired and processed to demonstrate the usefulness of the developed system along with its calibration procedure. The 2-D images generated in different frequency bands show that the dynamic range is about 40 dBsm for horizontal-horizontal (HH) and vertical-vertical (VV) polarizations, while it is around 30 dBsm for vertical-horizontal (VH) and horizontal-vertical (HV) polarizations. Meanwhile, the cross-polarization isolation of the developed system is better than 31 dBsm at the current state.

Index Terms— Millimeter radar imaging, multiple input multiple output (MIMO) radar, near-field radar measurement, polarimetric radar.

I. INTRODUCTION

MULTIPLE input multiple output (MIMO) radar systems have been developed for various applications, including autonomous driving [1], [2], [3], concealed threat detection [4], [5], [6], and target motion estimation [7], [8]. The MIMO radar can also be an effective instrument for the measurement of radar cross section (RCS) images to understand the scattering phenomenon of natural environment and the scattering characteristics of man-made targets [9], [10], [11].

In the state-of-the-art imaging measurement, the backscattering field data of an interested target is collected at different aspect angles through a wide frequency range to obtain 2-D or 3-D radar images [12], [13], [14]. Besides, after the successful applications of polarimetric radar in meteorology [15], [16], [17] and geoscience [18], [19], [20], [21], the measurement of

polarization scattering matrix (PSM) arouses more attention, as it characterizes the intrinsic features of targets, including material, composition, and structure, enabling target identification and recognition [22], [23], [24]. To satisfy the up-to-date requirements for the radar imaging measurement, several ideas can be adopted in the development of a MIMO imaging radar system. For a high resolution at down-range, a vector network analyzer (VNA) can be adopted as the signal source and the receiver of the radar system to achieve stable frequency sampling through an ultrawideband (UWB) with high sensitivity. The method for achieving a high resolution at cross-range in the MIMO radar imaging system is similar to that in synthetic aperture radar (SAR) imaging systems. Take the rail SAR as an example [25], [26]. The VNA is connected to an antenna installed on mobile platform for frequency data collection at numbers of aspect angles, which is equivalent to placing an antenna at each aspect angle to transmit and receive signal. To the same ends, an antenna array can be used as a replacement to implement electronic azimuth scanning without any extra complexity for data processing. This idea is further explored in the MIMO radar systems, where a virtual element array is formed by means of permutation and combination of transmitting and receiving antennas to reduce the number of antennas. Meanwhile, dual-polarized antennas can be used in the assemblage of the antenna array to develop a polarimetric MIMO radar system.

Except for the design of hardware architecture, other issues are involved in the development of a polarimetric MIMO radar system with desirable performance. For instance, as the transmitting power of the VNA-based MIMO radar system is relatively weak, the echo data is generally acquired at a close or standoff range under near-field condition, resulting in the spatial variation of point spread function (PSF) in 2-D radar imagery [9], [27]. Besides, the MIMO radar actually implements bistatic measurement rather than monostatic measurement [28], due to the fact that the transmitting and the receiving antennas are distributed in different positions.

The mentioned issues indicate two major challenges in the calibration of polarimetric MIMO radar systems for near-field UWB imaging measurement [29], i.e., 1) for each signal channel corresponding to a specific virtual element, the frequency sampling data should be compensated to alleviate the impacts of nonlinear signal distortion, which originates from the variable frequency responses of radio frequency (RF) electronic devices and 2) considering that a calibrator whose scattering characteristics are insensitive to bistatic angle, is required for

the precise compensation of channel consistency, dihedral and trihedral reflectors are not perfect calibrators for the near-field polarimetric MIMO calibration.

In contrast to the existing microchip-based MIMO radar systems which operate at a close range [30], [31], the inconsistent amplitudes and phases of the frequency responses among the signal channels cannot be compensated completely via cable length compensation alone. To improve system performance, the dihedral reflectors are generally used to calibrate polarimetric MIMO radar [32], [33]. However, as the PSMs of the dihedral calibrators vary with both frequency and bistatic angle, the MIMO radar data of the calibrators deviate from the theoretical values. Consequently, the calibration results are always represented as the SAR/Inverse Synthetic Aperture Radar (ISAR) images, which are compared to the human visualization for validation, rather than the RCS values, the dynamic ranges, or the cross-polarimetric isolation.

In our previous works, a MIMO radar system operating at microwave frequency bands was developed for near-field measurements in 2016 [9], while the system was upgraded with dual-polarized antennas in 2017 for near-field polarimetric measurements [29]. In this work, we intend to fabricate a polarimetric MIMO radar system operating at Ka frequency band spanning from 26.5 to 38 GHz for near-field imaging measurement. Due to the fact that the price of the dual-polarized UWB antennas is much higher than the single-polarized antennas under similar property, pairs of mutually perpendicular single-polarized antennas are adopted as the replacement to constitute the transmitting and receiving channels for different polarization modes in the PSM, involving horizontal-horizontal (HH), horizontal-vertical (HV), vertical-horizontal (VH), and vertical-vertical (VV). The former and the later letters stand for the polarization mode of the transmitting and the receiving antennas, respectively, which can be either horizontal (H) or vertical (V) polarization. For the system calibration, the rotatable double-antenna polarimetric active radar calibrator (RODAPARC) used in our previous polarimetric calibration [29], [34] is not available in this case, because of distinct operating frequency bands. Metal cylinders and a short ellipsoidal cylinder (SEC) [35] are used in the calibration HH and VV channels, whereas a plate dihedral with a specific rotation angle is selected as the calibrator for cross-polarization (HV and VH) channels. Regarding the bistatic scattering characteristics of the plate dihedral in near-field condition, the theoretical RCSs varying with frequency and azimuth angle are calculated for each element via the method of moments (MoM) [36]. The measurement data is compensated in reference to the calculated values at each frequency sampling point for all channels, while the measured and the simulated 2-D images generated through back projection (BP) are compared to improve the channel consistency for each polarization mode. In our test, the dynamic range of the developed millimeter MIMO radar is higher than 40 dBsm for HH and VV polarizations, and 30 dBsm for the cross-polarizations.

The major contribution of this article can be briefly summarized as the idea for compensating the inconsistent channel frequency response of the polarimetric MIMO radar system
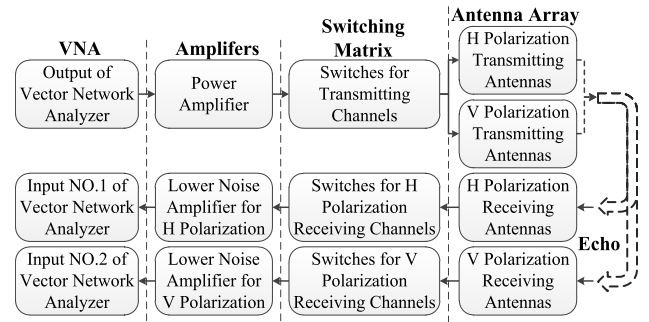

Fig. 1. Signal flow diagram of developed polarimetric MIMO radar system.

with the simulated echo signals of the calibrators. A few quantifiable criteria are given to demonstrate its usefulness, including the dynamic range and the cross-polarimetric isolation.

The remainder of the article is organized as follows. Section II presents the system architecture of the polarimetric MIMO radar, including the antenna array configuration and signal processing procedure. Data acquisition and system calibration are introduced in Section III, where the system calibration technique based on simulation data is proposed. Outdoor experimental results with analysis are given in Section IV, followed by a conclusion in Section V.

II. SYSTEM ARCHITECTURE OF POLARIMETRIC MIMO RADAR

The signal flow diagram of the polarimetric MIMO radar is shown in Fig. 1, where a VNA with four ports is selected as the signal source and the receiver for the system, including one output port for transmitter and two input ports for receivers. Each port is connected to an amplifier for a farther effective range, in which the amplifier in the transmitting branch has high saturation power at 1 dB compression point, whereas the amplifiers with a better noise figure are preferred in the receiving branch. Several single-pole multiple-throw RF switches are used to build a controllable switching matrix in the connection of the transmitter and the receivers to the corresponding antennas. The VNA and the switching matrix are connected to the same personal computer for time synchronization.

As it can be seen in Fig. 1, whatever the polarization is specified for the transmitting signal, the echo data is acquired simultaneously in the H and the V polarizations via two ports of the VNA. In this way, two rounds of data acquisition should be implemented to achieve full polarimetric data. Orthogonal waveform technique can be applied to acquire four polarizations simultaneously. However, the applicability will not be explored in this work, as the dynamic range of the 2-D images is prior to the imaging speed in our scope.

The sampling time of the VNA is related to the parameter settings, including the sweeping frequency bandwidth, the number of samples, the dwell time at each frequency point, and the average number of measurements. As the typical switching time of the RF mechanical switches is up to 15 μs, the duration time at each channel for frequency sampling is generally less than 1 s in our tests. Meanwhile, to achieve sufficient field size

at cross-range, the number of azimuthal sampling elements for each polarization is about 96 in our design. It takes several minutes to measure one set of full polarimetric MIMO data for a specific scene.

The down-range and cross-range resolutions of a uniform linear array can be calculated as follows:

$$\delta_r = \frac{c}{2B} \tag{1}$$

$$\delta_{cr} = \frac{\lambda_c}{2\theta_a} \approx \frac{\lambda_c R_0}{2L} \tag{2}$$

where δ_r and δ_{cr} are the down-range and the cross-range resolutions, respectively; c denotes the propagation speed of the electromagnetic signal, which is approximate to the speed of the light through the air; B is the imaging bandwidth; λ_c represents the center wavelength; θ_a denotes the aperture angle of the synthetic virtual array, which can be calculated with the reference distance R_0 and the synthetic aperture length L.

When the 2-D resolutions of the images are specified, the necessary number of samples at each dimension depends upon the expected size of the imaging area. The maximal blurred range along the down-range is related to the sampling interval in the given bandwidth, which is generally a constant for uniform frequency sampling. Consequently, the high-resolution range profiles (HRRPs) of the frequency sampling data can be generated efficiently by means of fast Fourier transform (FFT). For the cross-range dimension, the maximal azimuthal field size is related to the number of the virtual elements synthesized via the permutation and combination of the transmitting and the receiving antennas. The virtual elements are designed in a linearly uniform distribution to simplify the fabrication of the MIMO antenna array. The BP algorithm is adopted to generate 2-D images for nonuniform angle sampling. These designs will be discussed in Sections II-A–II-C.

A. Structure of MIMO Array

The MIMO array assembled with single-polarized antennas is shown in Fig. 2, where the smaller red rectangles and the larger blue rectangles represent the transmitting antennas and receiving antennas, respectively, while the lines and the shadows in the rectangles indicate the H polarization state and the V polarization state, respectively. The horizontal relative positions of the antennas are given in Fig. 2 with the letter d, which represents the horizontal interval between two adjacent receiving antennas. In contrast, the selection of the vertical intervals between two arbitrary lines of antennas is more flexible as long as the assembling condition can be satisfied, such as enough space for cable installation.

As it can be seen in Fig. 2, the virtual element arrays for four polarization modes are synthesized at different heights using eight transmitting and 12 receiving antennas. The synthetic aperture length of each array is 12.125d, which consists of 94 nonoverlapping virtual elements (96 in total). Except for the virtual elements at both ends of the synthetic arrays, the horizontal interval of the virtual elements is 0.125d.

The inner structure of the MIMO array is given in Fig. 3. As the length of the transmitting horn antennas is different
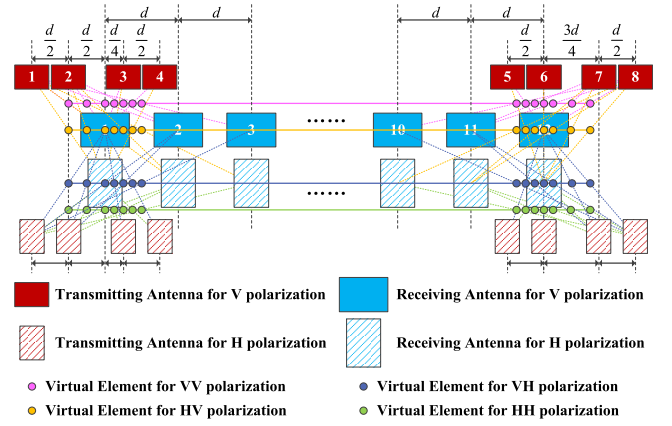

Fig. 2. Sketch of antenna distribution for MIMO array.
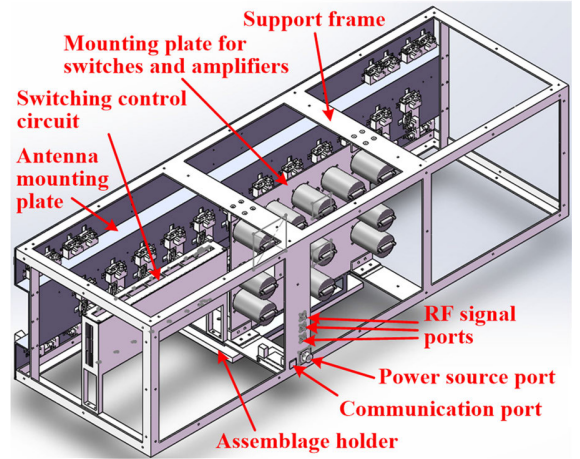

Fig. 3. Blueprint of inner structure for MIMO array without cables and wires.

from the receiving horn antennas, the mounting plate is curved to align the front surface of all the antennas. A support frame is attached to the antenna mounting plate for the prevention of mechanical deformation.

The frame provides a foundation for other parts, including the mounting plate for switches and amplifiers, the protection box for switching control circuit, the communication module, and the assemblage holder in connection with a turntable or a lifter. Meanwhile, cables and wires are fixed on the antenna mounting plate and the support frame in case of damage and loose junction owing to transportation.

After the protection shell of the MIMO array is assembled for package, only five ports remain on the panel, enabling convenient transportation, assembly, and application of the MIMO radar system.

B. Signal Processing Procedure for HRRP Generation

According to the typical scattering phenomenon of man-made targets, the total echo signal of an arbitrary target can be modeled as the coherent superposition of the scattered signals from a set of scattering centers. In the frequency domain, the echo signal of the kth virtual channel for each polarization can

be expressed as follows:

$$E_k(f) = U_k(f) \sum_{m=1}^{M} H_{k-m}(f) \sqrt{\sigma_m(f)} \exp\left(-j\frac{4\pi R_{k-m}}{c}f\right)$$

(3)

where E_k denotes the echo signal received by the kth virtual channel; f represents the frequency; M is the total number of scattering centers; R_{k-m} represents the distance from the kth virtual element to the mth scattering center; σ_m denotes the RCS of the mth scattering center, whose value is related to the frequency and the polarization mode; U_k represents the frequency spectrum of the transmitted signal in the kth channel, whose magnitude is approximate to a constant in the passing band for ideal linear frequency modulation (LFM) signals; and H_{k-m} is the frequency response of the kth channel to the mth scattering center, which can be characterized with three major components, i.e.,

$$H_{k-m}(f) = H_t(f, \theta_{kt-m}) H_r(f, \theta_{kr-m}) H_{kc}(f)$$

(4)

where H_t and H_r denote the frequency responses of the transmitting and the receiving antennas, which are different in the developed system in consideration of pattern, gain, and the angle deviation from the beam orientation; θ_{kt-m} and θ_{kr-m} are the deviation angles of the transmitting and the receiving antennas, respectively; and H_{kc} is the total frequency response of the RF devices constructing the kth channel, including the cables, the switches, the amplifiers, and the flanges.

As it can be seen from (3) and (4), when the channel frequency response H_{k-m} is constant in the passing band, the RCS distribution along the distance, namely, the HRRP, can be generated via the inverse FFT (IFFT) of the frequency samples for each channel. However, the response H_{k-m} of a real system is a complex number varying with the frequency and the antenna patterns, leading to the distortion of the generated HRRPs [37], [38].

To compensate the impacts of the channel frequency response, a calibrator with a single dominant scattering center and a known RCS characteristic can be placed at a certain distance to measure frequency data. The theoretical and the measured values are substituted into (3) to solve the compensation coefficient for each frequency sampling point. Due to the fact that the main beams of the transmitting and the receiving antennas are normally orientated at the target, the impacts of the antenna patterns on the channel frequency response are negligible. Based on this assumption, the solved coefficients are roughly equivalent to the total frequency response of the RF devices, i.e.,

$$H'_k(f) = K \frac{E'_{kc}(f)}{\sqrt{\sigma_c(f)}} \exp\left(j\frac{4\pi R_{kc}}{c}f\right)$$

(5)

where H'_k denotes the estimated frequency response of the kth channel; K is the gain coefficient irrelevant to frequency; E'_{kc} denotes the measured frequency data in the kth channel; σ_c represents the theoretical RCS profile of the calibrator varying with frequency; and R_{kc} is the equivalent propagation distance from the receiver to the calibrator for the kth channel, which is related to the physical distance from the MIMO array to
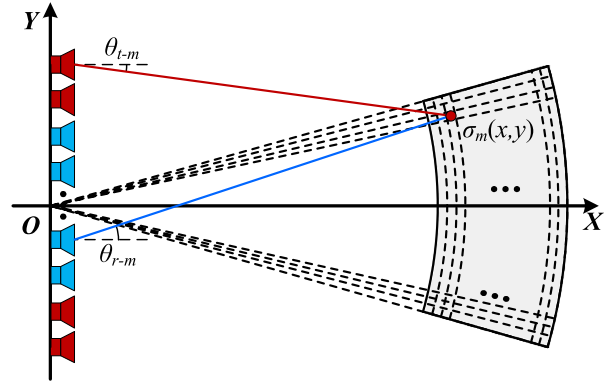

Fig. 4.   Coordinate illustration for 2-D imagery.

the calibrator as well as the electrical path length of the RF devices, especially the cables.

Note that the propagation speed of the electromagnetic signal through the cables is different from that through the air. To alleviate the impacts of the calibrator positioning accuracy on the response estimation, the equivalent length of the cables can be roughly calculated based on the designed cable length and the theoretical speed. After the rough compensation of the cable length, the distance of the calibrator can be estimated via searching the maximal position of the HRRP.

C. Signal Processing Procedure for 2-D Imagery

The coordination for the near-field 2-D imagery of the MIMO radar is given in Fig. 4, where the center of the MIMO array is set as the origin, while the antennas are distributed along the Y-axis. Under the near-field condition, the uniform frequency sampling and the uniform linear azimuthal sampling are equivalent to a sector ring in the spatial wave number domain, resulting in the cross-range resolution in (2) varying with the distance of the imaging area to the array.

The BP algorithm is used to achieve the cross-range resolution rather than the cross-range FFT. The processing procedure of the BP mainly includes four steps.

1) Generate the HRRP for the frequency data acquired in each channel.
2) Specify the imaging area which is meshed into grid points.
3) Calculate the distance from the grid points to each virtual element and generate 2-D complex data for the meshed grid via the interpolation of the corresponding HRRP.
4) Compensate a phase for the interpolated 2-D data and accumulate the compensated data from all channels, given as follows:

$$\sqrt{\hat{\sigma}(x,y)} = \sum_{k=0}^{K-1}\left[W_k\sqrt{\hat{\sigma}_k(x,y)}\exp\left(j\frac{4\pi R_k(x,y)}{c}f_c\right)\right]$$

(6)

where $(\hat{\sigma}(x,y))^{1/2}$ denotes the spatial distribution of the complex RCS, whose magnitude is normally named as the 2-D radar image; $(\hat{\sigma}_k(x,y))^{1/2}$ represents the 2-D complex

RCS image of the kth channel, which is obtained by the HRRP interpolation; $R_k(x, y)$ denotes the distance from the grid point (x, y) to the kth virtual element; f_c is the center frequency of the imaging spectral band; and W_k denotes complex compensation coefficient for the kth channel.

Although the channel compensation coefficient W_k can be used to suppress the cross-range sidelobes [9] in the method similar to digital beamforming, the major concern in this work is the improvement in the channel consistency and the 2-D image quality. According to the BP procedure, the quality of final images depends upon the compensation residuals of the frequency response and the channel consistency, which are related to several factors, including the bistatic and the aspect scattering characteristics of the calibrator, and the radiation pattern of the transmitting and receiving antennas.

An optimization problem about W_k can be established to minimize the difference between the measured image and the theoretical image, expressed as follows:

$$\min_{\{W_k\}} \left\| \sum_{k=0}^{K-1} \left[W_k \sqrt{\hat{\sigma}'_{ck}(x, y)} \exp\left(j \frac{4\pi R_k(x, y)}{c} f_c \right) \right] \right.$$
$$\left. - \sqrt{\hat{\sigma}_c(x, y)} \right\|$$
$$\text{s.t.} \sum_{k=0}^{K-1} \left(W_k W_k^* \right) = 1 \qquad (7)$$

where $(\hat{\sigma}'_{ck}(x, y))^{1/2}$ is the measured 2-D complex RCS image of the kth channel; $(\hat{\sigma}_c(x, y))^{1/2}$ denotes the simulated spatial distribution of the complex RCS; and symbols $||\cdot||$ and $*$ represent the norm operator and the conjugation operator, respectively.

Note that the channel consistency compensation has a negligible impact on the final images when the residual of the frequency response compensation is remarkably small. In this case, the coefficient W_k can be set as a constant.

D. Possible Upgrade for Polarimetric MIMO Radar

The developed MIMO radar can be upgraded in several aspects to improve measurement efficiency enabling applications in real-world scenarios and high dynamic environment.

1) As shown in Fig. 1, a VNA is employed as the LFM signal source as well as the receiver for the developed MIMO radar. A four-port VNA can be used to double the data acquisition speed. The expense is an additional transmitting channel connecting the VNA and the RF switch matrix, in which an additional amplifier should be assembled.

2) The VNA and the RF matrix can be replaced by a multiple channel receiver. In this way, the radar system can operate in single transmitting multiple receiving mode, where the RF matrix is simplified to control asynchronous transmitting only. The main challenge is the development of a receiver with enough synchronous channels, except for the structure complexity for additional RF devices, such as LNAs.

3) The MIMO radar can operate in multiple transmitting multiple receiving mode when the multiport transmitter
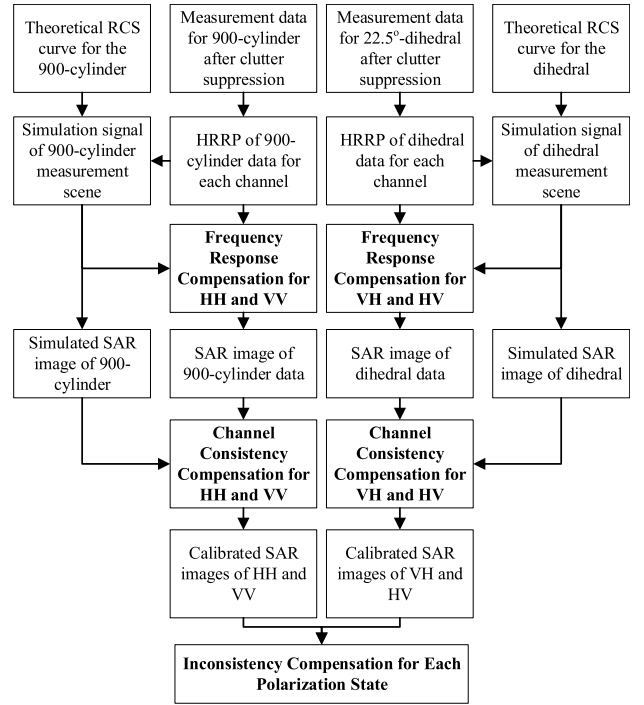

Fig. 5. Roadmap for MIMO system calibration.

and the multiport receiver are available along with suitable orthogonal waveform. The synchronization and orthogonality of the radar signals are major concerns in this case, involving the costs of the MIMO radar system.

For static scenarios and low dynamic environment, the major challenge for the implementation of the MIMO radar is the near-field condition, including the alignment of the MIMO array to the target, the spatial nonuniform irradiance of radar power, the spatial variation of PSF, and the grating lobes of the sparse virtual element array.

III. MEASUREMENT FOR MIMO SYSTEM CALIBRATION

The road map for the MIMO system calibration is given in Fig. 5, where the calibration procedure mainly consists of two steps including the frequency response compensation and the channel consistency compensation. In theory, the RCS value of a plate dihedral with a rotation angle of 22.5° is equal in the HH, VH, HV, and VV polarizations. However, the dihedral RCS is sensitive to bistatic and viewing angles, which vary with the virtual elements for the MIMO array. As a compromise, two sets of measured data are adopted in the proposed calibration procedure, i.e., the measured data of a 900-cylinder for the HH and VV polarizations and the measured data of a plate dihedral with a rotation angle of 22.5° for the VH and HV polarizations. The transmitting and receiving channels for the HH, VH, HV, and VV polarizations are respectively calibrated to generate images, while the absolute magnitudes of the scattering centers in the images are calibrated according to the RCS value of the 900-cylinder.

The developed MIMO radar system is deployed in a yard to acquire the necessary data for the proposed calibration procedure. The physical size of the array is about 1.0×0.5 m,

TABLE I
MEASUREMENT PARAMETERS FOR SYSTEM CALIBRATION

Parameters		Values
Radar system settings	Frequency sampling	26.5 to 38 GHz in step of 5MHz
	Azimuthal sampling	94 non-overlapping virtual elements in interval of 9mm
	Average number for each sample	4 times
	Hardware range gate	7m to 13m
	Average time for data acquisition	Less than 5 minutes for one set of full polarization data
Calibrator Selection	HH and VV polarization modes	A SEC located at (8, -1.5)* A 900 cylinder located at (10, 0)* A 750 cylinder located at (12, 2)*
	VH and HV polarization modes	A plate dihedral located at (10, 0)* with rotation angle of 22.5º

* Position in the XOY coordinate defined in Fig.4.

(a)

(b)

(c)

(d)

Fig. 6. Measurement scene photographs for MIMO radar system calibration. (a) Developed system. (b) Measurement for background clutter. (c) Measurement for HH and VV polarizations. (d) Measurement for VH and HV polarizations.

while the synthetic aperture is around 0.84 m. The measurement scene is shown in Fig. 6. The MIMO array is mounted on a turntable holder with a mobile lifter, while three plastic cuboids at a height of 1.6 m are placed in the measurement field as support for the calibrators. The MIMO array aiming at the center of the field is lifted to the same height as the calibrators. The major parameters for the data acquisition are listed in Table I. To alleviate the impacts of the clutter, the frequency response of the background echo signal is measured and cancelled before the implementation of the data processing procedure in Fig. 5.

According to the selected parameters in Table I, the maximal blurred range is 30 m involving the equivalent cable length of about 6.3 m. To alleviate the impacts of the intensive scattering from unexpected objects, the calibrators are placed at the area with relatively low background level, where a range gate is set to prevent the radiation leakage from other intensive objects, such as the walls of the yard. The background data is measured for the implementation of the constant clutter cancellation to obtain higher signal-to-noise ratio (SNR).

An SEC with a diameter of 38.1 cm (1500 mils) and a height of 17.78 cm [35], a cylinder with a diameter of 22.86 cm (900 mils) and a height of 10.67 cm, and a cylinder with a diameter of 19.05 cm (750 mils) and a height of 8.89 cm are selected as the calibrators for the HH and the VV polarizations, whereas a plate dihedral with a plate size of 10 × 7.5 cm is adopted for the VH and the HV polarizations. The RCS value of the SEC and the 750-cylinder can be used in the quantitative analysis on the calibration effectiveness.
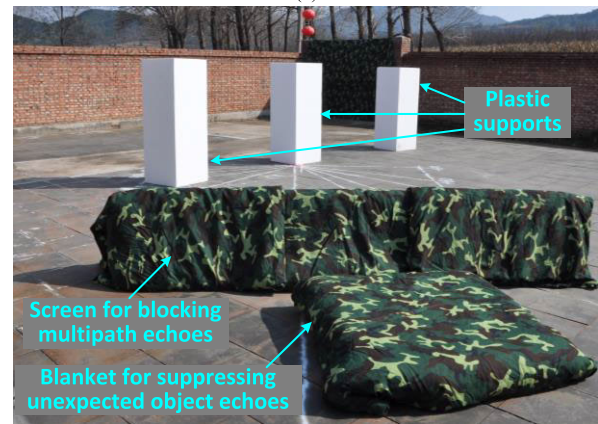
Under these specified conditions, the cross-range resolution at a center frequency of 32.5 GHz is around 4.2, 5.3, and 6.4 cm at the down-range of 8, 10, and 12 m, respectively, corresponding to an azimuthal field of 4, 5, and 6 m. When the band with a higher center frequency is used in the imagery, a better cross-range resolution can be achieved with a smaller azimuthal field. The system calibration procedure of different polarization modes will be discussed as follows.

A. Calibration for HH and VV Polarization Modes

Three calibrators are placed separately in the field to synthesize a more intensive target echo for higher signal-to-clutter ratio (SCR) and SNR. As the RCSs of the SEC and the two cylinders are insensitive to the azimuthal angle, their

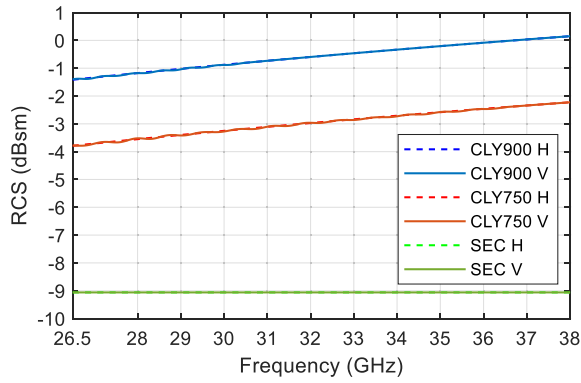Fig. 7. Theoretical RCS for 900-cylinder, 750-cylinder, and SEC in HH and VV polarizations.
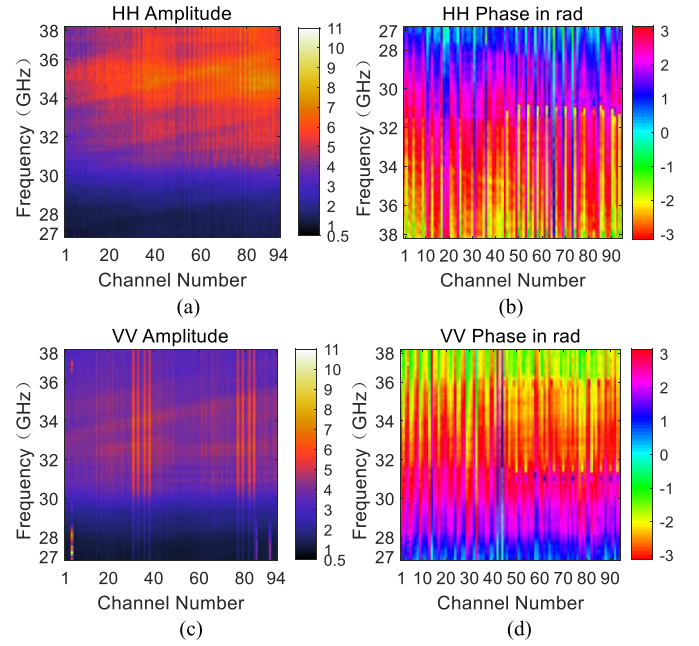

Fig. 8. Compensation coefficients for channel frequency responses in HH and VV polarizations. (a) Amplitude of HH polarization. (b) Phase of HH polarization. (c) Amplitude of VV polarization. (d) Phase of VV polarization.
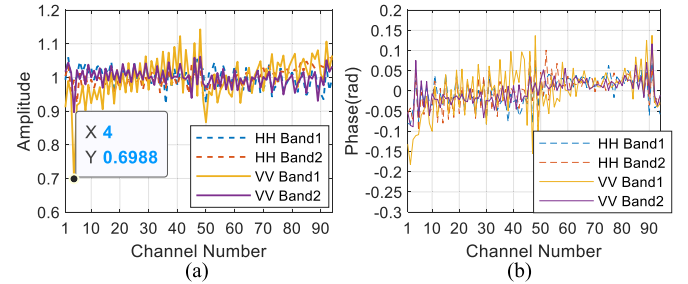

Fig. 9. Channel consistency compensation for HH and VV polarizations in 26.5–32.5 GHz (band 1) and 32–38 GHz (band 2). (a) Amplitude of compensation coefficients. (b) Phase of compensation coefficients.

theoretical RCS profiles varying with frequency are given in Fig. 7. For these three calibrators, their RCS values for the HH and the VV polarization modes have slight difference in the specified frequency spectrum, whereas their RCS values vary slowly with the frequency, enabling an accuracy estimation of their position in the specified coordinate through the search of local maxima in the HRRPs. In detail, the estimated position of the SEC, the 900 and the 750 cylinders, is respectively (8.205, −1.541), (10.193, −0.015), and (12.160, 1.960) in contrast to the specified values in Table I.

With the assumption of only one dominant scattering center for each calibrator, the echo signal of each channel can be simulated using the theoretical RCS profiles and the estimated positions. The simulated signals are compared to the measured data for the estimation of the compensation coefficient, which is the reciprocal of the channel frequency response H_k' in (5). The results are given in Fig. 8, where the horizontal axis represents the number of the selected virtual elements, which is assigned according to the Y-coordinate values in Fig. 4.

As it can be seen in Fig. 8, the compensation coefficient for the frequency response varies with both frequency (vertical axis) and channel (horizontal axis). The variation of compensation coefficients along with frequency is similar among all channels, because of similar synthetic frequency characteristics of the RF devices, especially amplifiers, switches, and cables. In short, the total channel gain is lower at higher frequency, while the magnitude of the total channel response is stronger for VV than that for HH at the specific frequency. Besides, the pattern and the gain of the transmitting and receiving antennas also contribute to the difference in channel frequency response. For instance, the eight bright lines in Fig. 8(c) correspond to a common receiving antenna, whose gain is remarkably different from others.

Note that the channel consistency in (6) can be compensated in the processing of the frequency response. When the echo signal is accurately simulated in accordance with the data measured under a high SNR level, the frequency response compensation executed independently in each channel is sufficient for high quality imagery.

To demonstrate the effectiveness of the compensation procedure, two frequency bands covering the whole frequency data are selected to generate the 2-D images of the calibrators,

i.e., 26.5–32.5 GHz (band 1) and 32–38 GHz (band 2). The corresponding compensation coefficients of the channel consistency for the HH and the VV polarization modes are given in Fig. 9, where the blue and the red dash lines describe the HH polarization for the two bands, while the yellow and the purple solid lines depict the VV polarization.

As it can be seen in Fig. 9, the coefficients for the channel consistency have slight difference to each other, except for several special channels, such as the fourth channel of the VV band 1, where the amplitude of the frequency response fluctuates remarkably as shown in the left bottom of Fig. 8(c). In Fig. 9(b), the maximal deviation of the coefficient phase is less than 0.2 rad, which is equivalent to around 1/32 of the wavelength. Consequently, the channel consistency compensation has negligible impacts on the quality of the 2-D images for the HH and the VV polarization modes in these two specified bands.

The calibration results of the two bands are given respectively in Figs. 10 and 11, where (a) and (b) denote the images of the raw data and the compensated data. The dynamic range is set as 45 dBsm for each image in reference to the
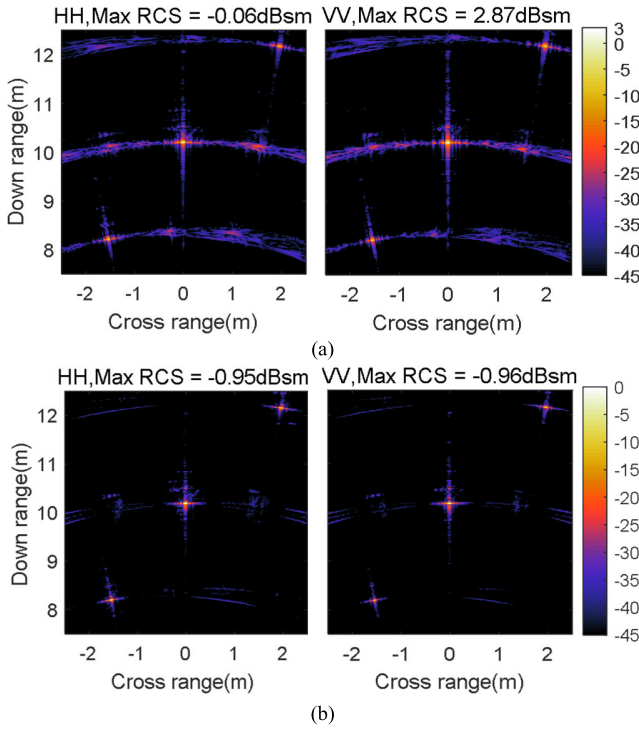
Fig. 10. Results of MIMO system calibration in 26.5–32.5 GHz (band 1) for HH and VV polarizations. (a) Raw images. (b) Compensated images.
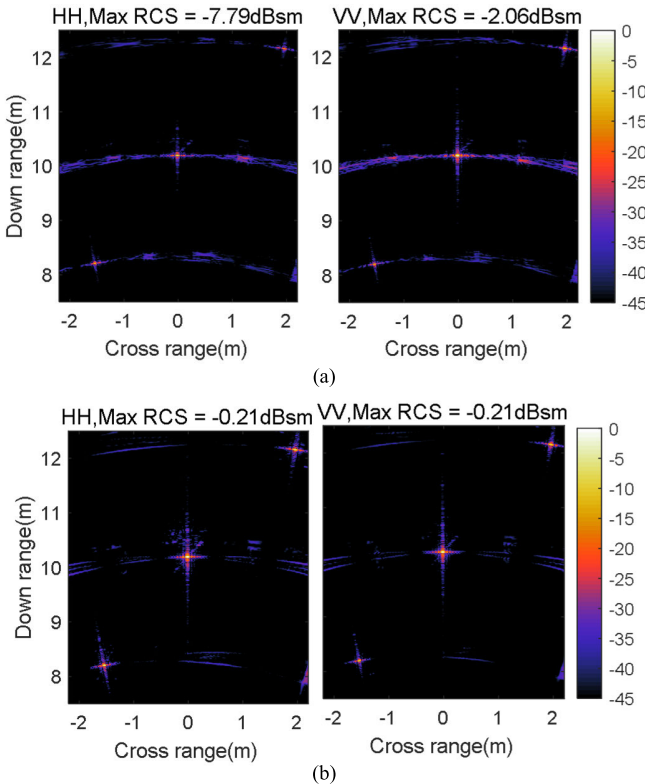

Fig. 11. Results of MIMO system calibration in 32–38 GHz (band 2) for HH and VV polarizations. (a) Raw images. (b) Compensated images.

respective maximal value. The defocus can be clearly observed in Figs 10(a) and 11(a), where the peaks of the scattering centers are attenuated, while the azimuth sidelobes can stain a wide area at the cross-range. After the compensation depicted

TABLE II
STATISTICS OF RCS VALUES IN 2-D IMAGES FOR CALIBRATORS

Channels		SEC in dBsm	900-Cylinder in dBsm	750-Cylinder in dBsm
Band 1 26.5-32.5GHz	HH	-5.303	-0.953	-7.961
	VV	-8.565	-0.959	-8.691
Band 2 32-38GHz	HH	-4.844	-0.209	-6.907
	VV	-9.502	-0.209	-8.611

in Figs. 10(b) and 11(b), the refocused images are similar to the simulated images as expected.

Note that the maximal value in each image corresponds to the specular scattering of the 900-cylinder, whose value is approximate to the average of the RCS profiles through the specified frequency range in Fig. 7. The absolute RCS values of the SEC and the 750-cylinder can be read from the compensated images, as listed in Table II.

The calibrator RCSs in the 2-D images are different from the theoretical values for various reasons, among which three major factors should be mentioned.

1) The distance of the calibrator to the MIMO array. According to the radar equation, the power of the echo is related to the distance. With reference of 10 m, the magnitude of the 750-cylinder specular scattering is about 3.288 dBsm lower than the theoretical value, whereas the magnitude of the SEC should be around 3.468 dBsm higher.

2) The pattern of the transmitting and receiving antennas. The half power beam widths are 30° and 18° for the transmitting and the receiving antennas, respectively. As shown in the images, the azimuth angles of the SEC and the 750-cylinder are 10.6° and 9.2°, resulting in a 2–3 dBsm decrease in the echo magnitude compared with the center 900-cylinder.

3) The electromagnetic scattering interaction between the calibrators and the plastic supports. The scattering of the plastic supports can be clearly seen around the 900-cylinder, as shown in the compensated images of Figs. 9 and 10. The RCS values of the calibrator pixels are enlarged because of the coupling scattering of the calibrators and the supports. This phenomenon is more significant for the HH than the VV, as the clutter scattering is more intensive in the HH polarization.

The method for the precise measurement of absolute RCS values is beyond the scope of this article. Instead, the system calibration for cross-polarization modes will be introduced.

B. Calibration for VH and HV Polarization Modes

The data of a plate dihedral placed at (10, 0) with a rotation angle of 22.5° is acquired for the calibration of the cross-polarization channels, as the parameters listed in Table I. Regarding the measurement data, the estimated position of the dihedral is (10.195, 0.016), which is used to calculate its RCS using the MoM under near-field condition. The calculation can be implemented via mature commercial software, including Altair FEKO and CST Studio Suite. The results of VH and HV polarization modes are given in Fig. 12.
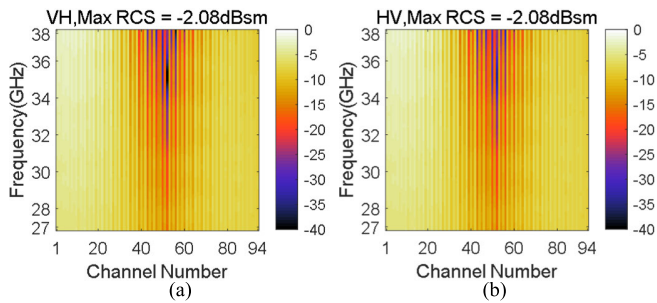
Fig. 12. Calculated near-field RCS for plate dihedral with rotation angle of 22.5° placed at specified position. (a) VH polarization. (b) HV polarization.

In theory, the four scattering components are equal for the dihedral with 22.5° rotation angle. Thus, the slight difference in Fig. 12(a) and (b) is negligible in most frequency points and channels. However, an obvious decrease in the RCS magnitude can be observed in the channels corresponding to larger bistatic angles, especially at higher frequency region. This phenomenon is different from the RCS curves of the SEC or the cylinders shown in Fig. 7. The sensitivity of the dihedral RCS to the azimuth and the bistatic angles has adverse impacts on the MIMO system calibration.

The solved compensation coefficients for the channel frequency responses in the VH and the HV polarization modes are given in Fig. 13, where the amplitudes of the coefficients are depicted in logarithmic values due to its wide range. The ridges in Fig. 13(a) and (c) indicate that the real dihedral attitude is different from the adopted assumption in the simulation, i.e., the dihedral does not precisely orient at the center of the MIMO array because of the setting error. Due to the fact that the dihedral attitude can hardly be either measured or estimated, only the phases of the coefficients are used to compensate the frequency responses for processing robustness in case of uncertain aiming accuracy.

Fig. 14 shows the channel consistency compensation for the VH and the HV polarization modes in 26.5–32.5 GHz and 32–38 GHz, respectively. As it can be seen, the amplitude of the compensation coefficient in the channels 1–47 is higher than that in the channels 48–94, indicating that the dihedral is placed nearly at the symmetric line of the MIMO array, whereas its orientation deviates from the symmetric line with a small intersection angle. Consequently, the compensation coefficient for the channel consistency tries to steer the orientation of the synthetic wave beam in accordance with the simulation data.

The calibration results of the two bands for the two cross-polarization modes are given respectively in Figs. 15 and 16, where (a) and (b) denote the images of the raw data and the compensated data. The magnitude range is set as −45 to −5 dBsm for all images. The defocus is alleviated after the compensation processing. However, the sidelobes in the compensated images of the cross-polarization modes are higher than those in the HH and the VV polarization modes, because the scattering radiation of the dihedral is much weaker for the virtual elements with larger bistatic angles. As shown in Fig. 12, the near-field bistatic phenomenon is severe at higher frequency, leading to a higher sidelobe level in band
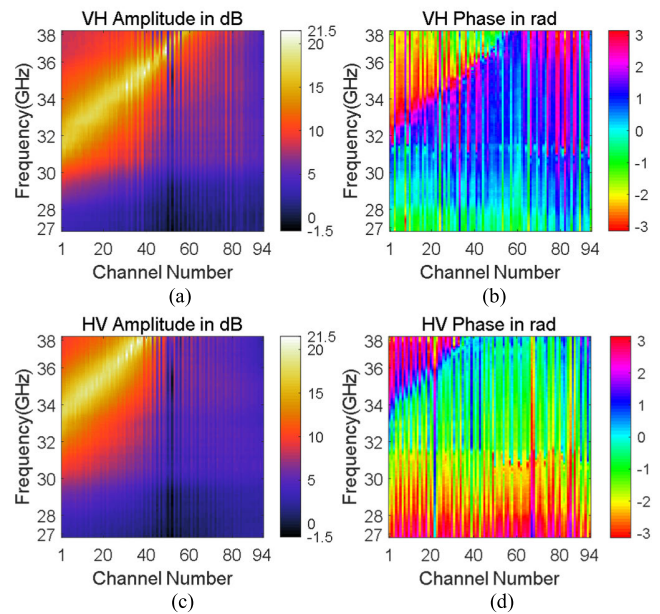

Fig. 13. Compensation coefficients for channel frequency responses in VH and HV polarizations. (a) Amplitude of VH polarization. (b) Phase of VH polarization. (c) Amplitude of HV polarization. (d) Phase of HV polarization.
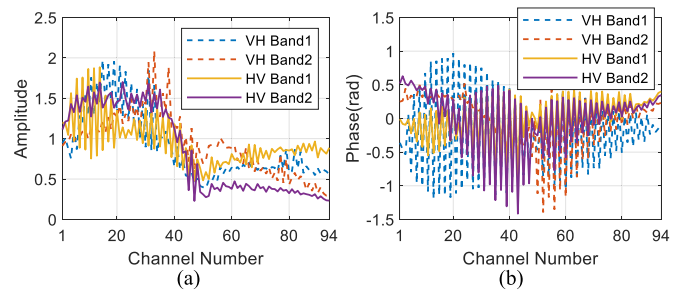

Fig. 14. Channel consistency compensation for VH and HV polarizations in 26.5–32.5 GHz (band 1) and 32–38 GHz (band 2). (a) Amplitude of compensation coefficients. (b) Phase of compensation coefficients.

2 compared with that in band 1. In detail, the sidelobe level in band 1 is about 35 dBsm in comparison with 30 dBsm in band 2, as depicted in Figs. 15(b) and 16(b).

Another issue for cross-polarization measurement is the definition of the absolute RCS value for the 2-D images. In the view of imagery, the magnitude of each pixel corresponds to the average among all channels, which can fluctuate dramatically in the bistatic cross-polarization measurement for the calibrators, such as the dihedral shown in Fig. 12. Although the compensation procedure is effective in the system calibration of the MIMO imaging radar, the polarimetric calibration for the accurate RCS measurement is still a great challenge at the current state.

To calibrate the magnitude difference, the dihedral images of the HH and the VV polarization modes are generated using the compensation coefficients in Section III-A, as shown in Fig. 17. As the four elements in the theoretical PSM of the 22.5° dihedral are equal, the magnitudes of either HH or VV image can be used as the reference to improve magnitude consistency of the VH and the HV images. Due to the fact that the intensive clutter in the HH polarization
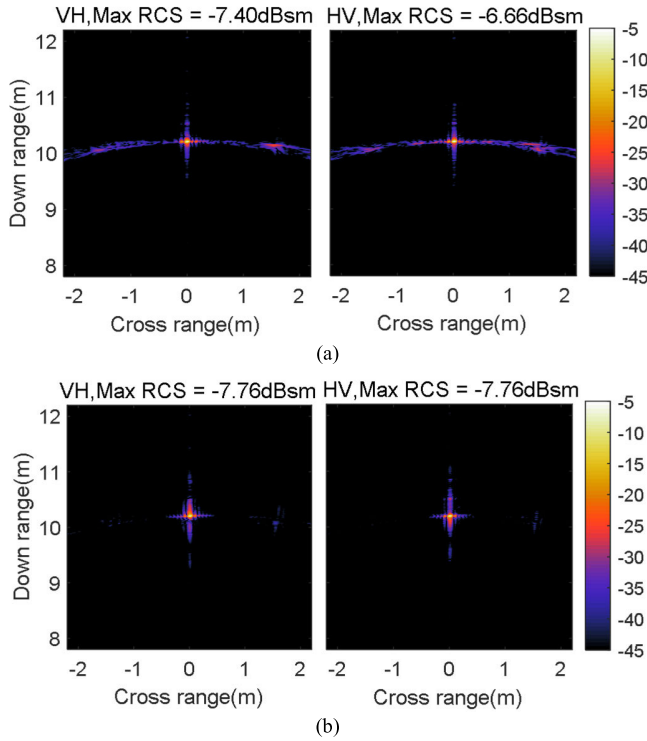
Fig. 15. Results of MIMO system calibration in 26.5–32.5 GHz (band 1) for VH and HV polarizations. (a) Raw images. (b) Compensated images.
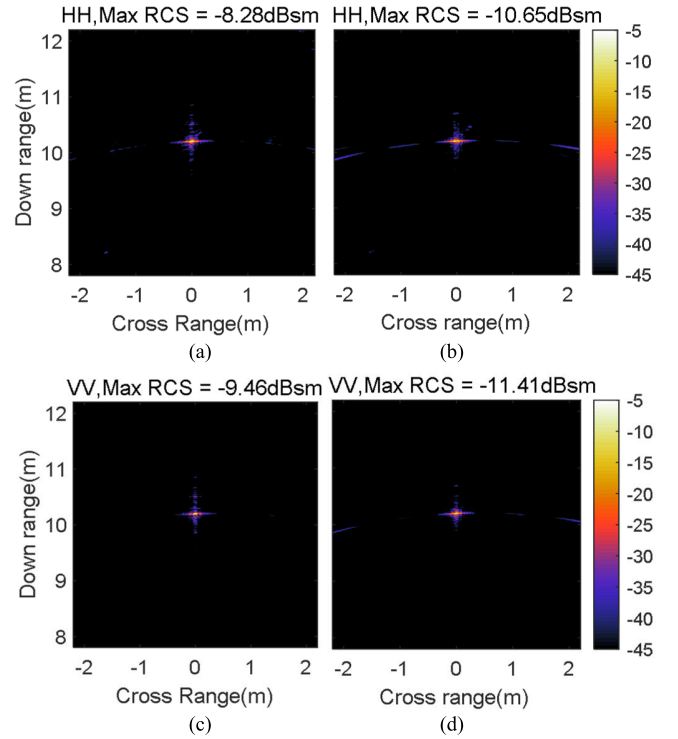

Fig. 16. Results of MIMO system calibration in 32–38 GHz (band 2) for VH and HV polarizations. (a) Raw images. (b) Compensated images.

Fig. 17. Compensated images of dihedral. (a) HH, band 1 (26.5–32.5 GHz). (b) HH, band 2 (32–38 GHz). (c) VV, band 1. (d) VV, band 2.
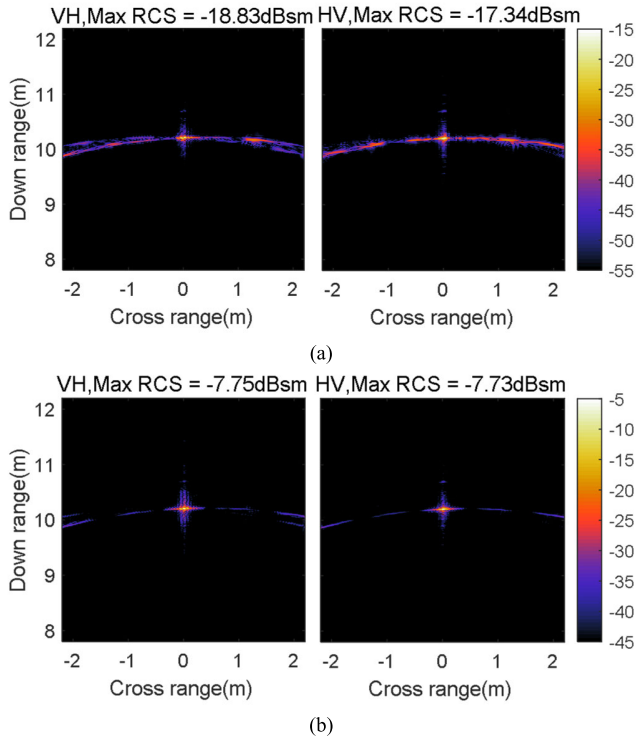
3.68 dBsm for the cross-polarization images in band 1 and band 2, respectively.

C. Discussion About Proposed Calibration Procedure

For the rigor of the data measurement, the calibration procedure should be executed for the MIMO radar system before each measurement experiment. When the parameter settings in Table I are adopted, one set of full polarimetric data can be acquired within 5 min. The total time for acquiring and processing three sets of data for the system calibration is less than 20 min, which is acceptable to implement recalibration every day.

It should be noted that the calibration procedure can be executed in a less rigorous way, i.e., the calibrator can be placed within the field of view of the MIMO radar along with the target, whose distance is far enough to ignore the couple scattering. In this way, the scattering center of the calibrator can be separated by means of digital signal processing enabling the execution of the procedure in Fig. 5. The effectiveness depends upon the SCR of the calibrator echo, which can be improved via static background suppression.

According to our experience, the calibration coefficients solved from the data measured in September 2021 can be directly used to process the data measured in May 2023 with a slight difference in the new coefficients. The stability of the radar system contributes to the stable frequency responses of the RF components. The signal source and the receiver of our MIMO radar system is the VNA, whose frequency response keeps steady for years. The frequency responses of passive devices, including the cables, the antennas, and

leads to overcompensation listed in Table II, the VV image is adopted in our application. In detail, the magnitude of the channel consistency compensation will be reduced by 1.7 and
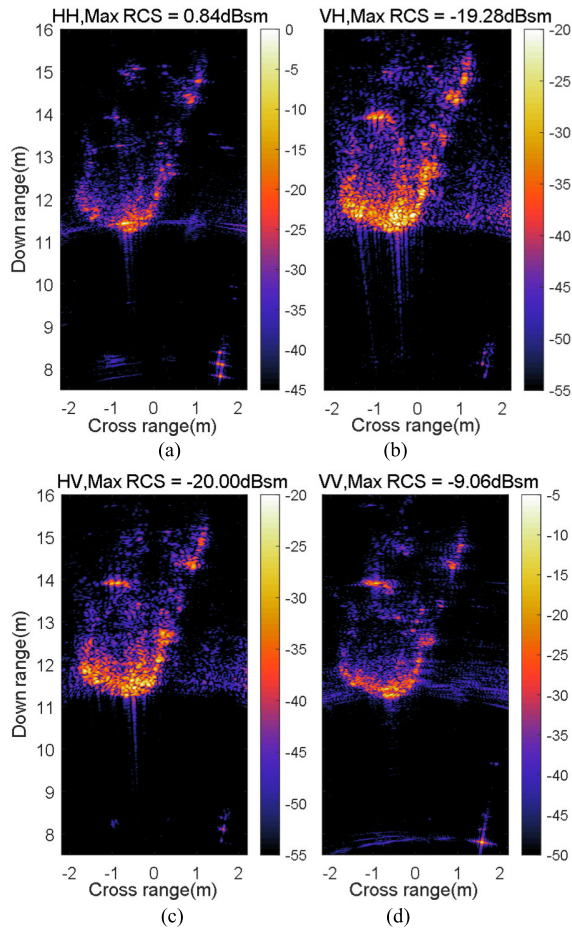
Fig. 18. Photograph of measurement scene for a Volvo XC90.

Fig. 19. Full polarimetric imaging results for Volvo XC90 in band 1 (26.5–32.5 GHz). (a) HH. (b) VH. (c) HV. (d) VV.

Fig. 20. Full polarimetric imaging results for Volvo XC90 in band 2 (32–38 GHz). (a) HH. (b) VH. (c) HV. (d) VV.

IV. MEASUREMENT FOR COMPLEX TARGET

To demonstrate the usefulness of the developed system and the proposed system calibration procedure, the full polarimetric data of vehicles is acquired in the same yard without constant background cancellation. The MIMO array is lifted to a height of about 2 m with a pitch angle of around 9.3°, enabling the synthetic wave beam pointing at down-range to be about 12.2 m, where a Volvo XC90 is expected to appear. To evaluate the scattering magnitude of the XC90, the SEC is selected as the calibrator for the HH and the VV polarization modes instead of the cylinders considering their different scattering characteristics varying with the pitch angle. The magnitude of the cross-polarization images can be deduced according to the relation discussed in Section III-B. The SEC is placed at the coordinate (8, 1.5) on a plastic supported at a height of 1 m, whereas the hardware range gate is adjusted at 7–16 m. Fig. 18 shows the photograph of the scene, while the 2-D MIMO images of band 1 (26.5–32.5 GHz) and band 2 (32–38 GHz) are given in Figs. 19 and 20, respectively. Figs. 19 and 20(a)–(d) represent HH, VH, HV, and VV polarization modes, respectively. The dynamic range is set at about 45 dBsm for the HH and the VV polarization modes, and 35 dBsm for the VH and the HV polarization modes.

the switches, have a slight change during their operating life. The performance of other active devices involving the RF amplifier and the LNAs is sensitive to temperature and fluctuating electricity supply, which can be maintained stably via installing assistive devices, such as heat sinks, cooling fans, and stabilized voltage supply.

Theoretically, the MIMO radar system has to be recalibrated when any one of the RF device's warranty is over or is replaced by a new one. However, no research has been done on the precise expiration date of the calibration coefficients. As the calibration data can be obtained and processed within an acceptable short period, it is a rational suggestion that the MIMO radar should be recalibrated for each measurement experiment which lasts days or weeks.
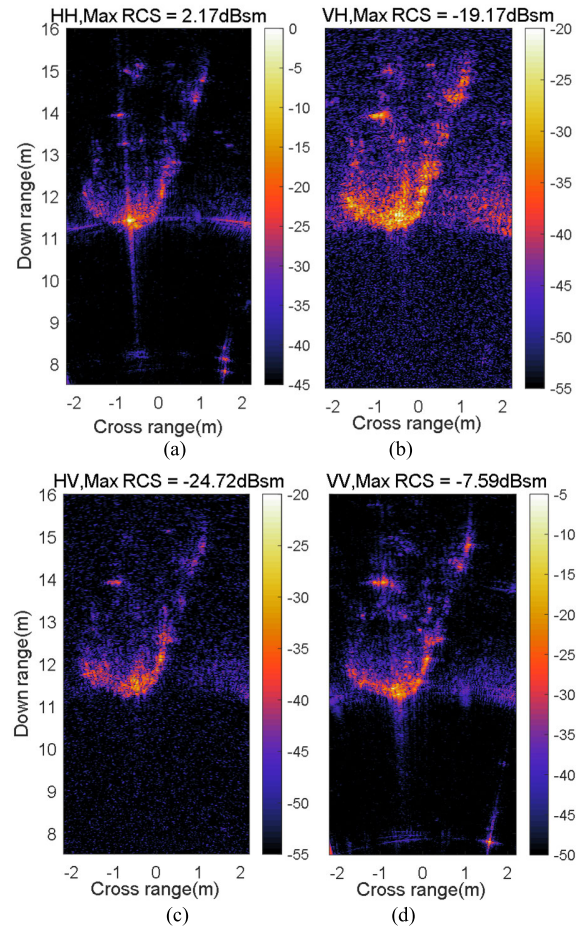
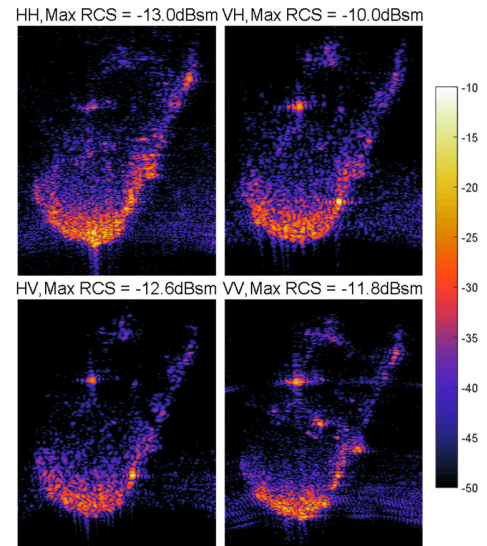Fig. 21. Full polarimetric imaging results for Volvo XC90 in 26.5–38 GHz. (a) HH. (b) VH. (c) HV. (d) VV.

Fig. 22. Full polarimetric imaging results for Mazda CX4 in 26.5–38 GHz.

The whole spectral (26.5–38 GHz) data can be used to generate full polarimetric 2-D images, as shown in Fig. 20. The down-range resolution is improved from 2.5 to 1.3 cm, which is about one-fifth of the cross-range resolution. The wider imaging bandwidth will bring out negligible benefits for the dynamic range of the images, which is about 40 dBsm for the HH and the VV images, while around 30 dBsm for the cross-polarization images using the current processing procedure.

Note that the scattering from the ground bricks can be observed at the down-range area from 7 to 9 m in the VV image as shown in Fig. 21(d), whose dynamic range is set as 60 dBsm. This phenomenon demonstrates that the dynamic range depends upon the sidelobe level of the most intensive scattering center appearing in the imaging area, which can be suppressed by means of spectrum filtering and super resolution processing.

In the end of this section, a set of full polarimetric 2-D images of a Mazda CX4 is given in Fig. 22, which is measured under the same condition as in Fig. 18. The maximal magnitudes of the four polarization images are quite similar to each other with the difference less than 3 dBsm. Thus, the four images can be depicted with the same color map to analyze scattering characteristics. As the height of the CX4 is different from the XC90, the scattering centers of the multipath effect can be separated in Fig. 22, where a block of intensive scattering area can be observed in the HH subimage in comparison with the VV subimage. The blur in the HH image provides circumstantial evidence for the decrease in maximal magnitude.

It can be seen that the maximal RCS value in the HH image is much higher than that in the VV image because of the multipath effect, which can be manifested by the three scattering centers behind the specular scattering center of the SEC. The multiple scattering between the XC90 and the ground accumulated in front of the vehicle results in an intensive scattering center similar to a corner reflector. Although the ground reflectivity is larger in the HH polarization, it is a coincidence that the multipath scattering centers appear at close down-range and cross-range cells to form that remarkably intensive scattering center.

Due to the reason that the theoretical cross-polarization RCS of the SEC is equal to zero, the magnitude of the specular scattering center of the SEC in the cross-polarization images can be used to identify the cross-polarization isolation of the system, which is about 31 dBsm.

It should be noticed that the SEC cannot be observed in Fig. 20(b) and (c), because of the low SNR at high frequency, which validates the results in Section III, i.e., the total channel gain decreases with the increase in frequency because the propagation attenuation through RF device is higher, especially the RF cables. Consequently, the dynamic range is limited by the SNR instead of SCR at high frequency, which can be improved by means of pulse accumulation at the expense of longer measurement duration.

V. CONCLUSION

Full polarimetric millimeter MIMO radar system operating at frequency spanning from 26.5 to 38 GHz is designed and developed to measure near-field radar images for scientific study. The MIMO antenna array is configured with pairs of single-polarization horn antennas to synthesize linear array involving 94 nonoverlapping virtual elements for each

polarization. The MIMO array is connected to a four-port VNA through a set of RF switches and several amplifiers, enabling the adjustable resolution and effective range along the down-range. The system flexibility is further improved via mounting the array on a mobile lifting turntable to provide data measurement at different aspect angles. The data of several selected calibrators is acquired in a specified yard to calibrate the system, in which the two metal cylinders and one SEC are used for the HH and the VV polarization modes in contrast to the plate dihedral for the two cross-polarization modes.

To ensure the quality of the acquired 2-D radar images, the system calibration procedure is implemented among each set of polarization channels independently, involving two major steps, i.e., frequency response compensation and channel consistency compensation. The former is executed for each channel through the point-to-point comparison of the measured data to the theoretical simulation results, whereas the latter is accomplished in the BP-based 2-D imagery via the calculation of a set of weight coefficients to minimize the difference between the measurement and the simulation images. In our tests, as the calibration process can be accomplished within 20 min, the MIMO radar system was calibrated at the beginning of each measurement experiment schedule.

To demonstrate the usefulness of the developed system along with the proposed system calibration procedure, the system is used to acquire and generate the 2-D images of the vehicles in various frequency bands. The generated images of the Volvo XC90 and the Mazda CX4 show that the dynamic range is 40 dBsm for the HH and the VV polarization modes, and 30 dBsm for the VH and the HV polarization modes. At the current state, the cross-polarization isolation is better than 31 dBsm for the developed system. As it can be seen, the developed system can be used to acquire full polarimetric near-field radar images in millimeter wave frequency band spanning from 26.5 to 38 GHz, enabling its applicability as an effective instrument for near-field scattering diagnosis.

At the current state, the system can obtain one set of full polarimetric data within 5 min, which is suitable for the measurement in a relatively static scenario. Hardware upgrade is necessary to adapt for dynamic or rapidly changing environments, such as the multiport transmitter, the multiport receiver, and the orthogonal waveform generator. Each of the updates involves technologic and economic challenges, which deserve further exploration.

REFERENCES

[1] Z. Peng and C. Li, "A portable K-band 3-D MIMO radar with nonuniformly spaced array for short-range localization," *IEEE Trans. Microw. Theory Techn.*, vol. 66, no. 11, pp. 5075–5086, Nov. 2018.

[2] A. Ganis et al., "A portable 3-D imaging FMCW MIMO radar demonstrator with a 24×24 antenna array for medium-range applications," *IEEE Trans. Geosci. Remote Sens.*, vol. 56, no. 1, pp. 298–312, Jan. 2018.

[3] A. Sayin, S. Pooni, E. Hoare, and M. Antoniou, "MIMO array for short-range, high-resolution automotive sensing," *IET Radar, Sonar Navigat.*, vol. 12, no. 10, pp. 1165–1171, Oct. 2018.

[4] B. Cheng et al., "340-GHz 3-D imaging radar with 4Tx-16Rx MIMO array," *IEEE Trans. Terahertz Sci. Technol.*, vol. 8, no. 5, pp. 509–519, Sep. 2018.

[5] J. Gao et al., "Fast three-dimensional image reconstruction of a standoff screening system in the terahertz regime," *IEEE Trans. Terahertz Sci. Technol.*, vol. 8, no. 1, pp. 38–51, Jan. 2018.

[6] M. Kowalski and M. Kastek, "Comparative studies of passive imaging in terahertz and mid-wavelength infrared ranges for object detection," *IEEE Trans. Inf. Forensics Security*, vol. 11, no. 9, pp. 2028–2035, Sep. 2016.

[7] Z. Hu, W. Wang, and F. Dong, "MIMO radar accurate imaging and motion estimation for 3-D maneuvering ship target," *IEEE Trans. Instrum. Meas.*, vol. 70, pp. 1–12, 2021.

[8] Q. Zheng et al., "A target detection scheme with decreased complexity and enhanced performance for range-Doppler FMCW radar," *IEEE Trans. Instrum. Meas.*, vol. 70, pp. 1–13, 2021.

[9] Y. Liu, X. Xu, and G. Xu, "MIMO radar calibration and imagery for near-field scattering diagnosis," *IEEE Trans. Aerosp. Electron. Syst.*, vol. 54, no. 1, pp. 442–452, Feb. 2018.

[10] D. Bleh et al., "W-band time-domain multiplexing FMCW MIMO radar for far-field 3-D imaging," *IEEE Trans. Microw. Theory Techn.*, vol. 65, no. 9, pp. 3474–3484, Sep. 2017.

[11] D. Tarchi, F. Oliveri, and P. F. Sammartino, "MIMO radar and ground-based SAR imaging systems: Equivalent approaches for remote sensing," *IEEE Trans. Geosci. Remote Sens.*, vol. 51, no. 1, pp. 425–435, Jan. 2013.

[12] T. Ikaheimonen, "Measurement of radar spurious emission with high dynamic range and optimized measurement time," *IEEE Trans. Instrum. Meas.*, vol. 60, no. 3, pp. 1010–1016, Mar. 2011.

[13] J. W. Odendaal and J. Joubert, "Radar cross section measurements using near-field radar imaging," *IEEE Trans. Instrum. Meas.*, vol. 45, no. 6, pp. 948–954, 1996.

[14] T. E. Tice, "An overview of radar cross section measurement techniques," *IEEE Trans. Instrum. Meas.*, vol. 39, no. 1, pp. 205–207, 1990.

[15] E. Barcaroli, A. Lupidi, L. Facheris, F. Cuccoli, H. Chen, and C. V. Chandra, "A validation procedure for a polarimetric weather radar signal simulator," *IEEE Trans. Geosci. Remote Sens.*, vol. 57, no. 1, pp. 609–622, Jan. 2019.

[16] C. Fulton et al., "Cylindrical polarimetric phased array radar: Beamforming and calibration for wether applications," *IEEE Trans. Geosci. Remote Sens.*, vol. 55, no. 5, pp. 2827–2841, May 2017.

[17] M. Galletti, D. H. O. Bebbington, M. Chandra, and T. Borner, "Measurement and characterization of entropy and degree of polarization of weather radar targets," *IEEE Trans. Geosci. Remote Sens.*, vol. 46, no. 10, pp. 3196–3207, Oct. 2008.

[18] O. Ponce, P. Prats-Iraola, R. Scheiber, A. Reigber, and A. Moreira, "First airborne demonstration of holographic SAR tomography with fully polarimetric multicircular acquisitions at L-band," *IEEE Trans. Geosci. Remote Sens.*, vol. 54, no. 10, pp. 6170–6196, Oct. 2016.

[19] Y. Yamaguchi, "Disaster monitoring by fully polarimetric SAR data acquired with ALOS-PALSAR," *Proc. IEEE*, vol. 100, no. 10, pp. 2851–2860, Oct. 2012.

[20] H. Wakabayashi, T. Matsuoka, K. Nakamura, and F. Nishio, "Polarimetric characteristics of sea ice in the sea of Okhotsk observed by airborne L-band SAR," *IEEE Trans. Geosci. Remote Sens.*, vol. 42, no. 11, pp. 2412–2425, Nov. 2004.

[21] M. A. Sletten and D. B. Trizna, "An ultrawideband, polarimetric radar for the study of sea scatter," *IEEE Trans. Antennas Propag.*, vol. 42, no. 11, pp. 1461–1466, Nov. 1994.

[22] J. Duan, L. Zhang, M. Xing, Y. Wu, and M. Wu, "Polarimetric target decomposition based on attributed scattering center model for synthetic aperture radar targets," *IEEE Geosci. Remote Sens. Lett.*, vol. 11, no. 12, pp. 2095–2099, Dec. 2014.

[23] L. Zhang, B. Zou, H. Cai, and Y. Zhang, "Multiple-component scattering model for polarimetric SAR image decomposition," *IEEE Geosci. Remote Sens. Lett.*, vol. 5, no. 4, pp. 603–607, Oct. 2008.

[24] R. Touzi, "Target scattering decomposition in terms of roll-invariant target parameters," *IEEE Trans. Geosci. Remote Sens.*, vol. 45, no. 1, pp. 73–84, Jan. 2007.

[25] Z. Yuan et al., "An approach to wide-field imaging of linear rail ground-based SAR in high squint multi-angle mode," *J. Syst. Eng. Electron.*, vol. 31, no. 4, pp. 722–733, Aug. 2020.

[26] G. L. Charvat, L. C. Kempel, and C. Coleman, "A low-power high-sensitivity X-band rail SAR imaging system," *IEEE Antennas Propag. Mag.*, vol. 50, no. 3, pp. 108–115, Jun. 2008.

[27] X. Xu and R. M. Narayanan, "Enhanced resolution in SAR/ISAR imaging using iterative sidelobe apodization," *IEEE Trans. Image Process.*, vol. 14, no. 4, pp. 537–547, Apr. 2005.

[28] R. E. Kell, "On the derivation of bistatic RCS from monostatic measurements," *Proc. IEEE*, vol. 53, no. 8, pp. 983–988, Jun. 1965.

[29] L. Kong and X. Xu, "Calibration of a polarimetric MIMO array with horn elements for near-field measurement," *IEEE Trans. Antennas Propag.*, vol. 68, no. 6, pp. 4489–4501, Jun. 2020.

[30] J. W. Smith, M. E. Yanik, and M. Torlak, "Near-field MIMO-ISAR millimeter-wave imaging," in *Proc. IEEE Radar Conf.*, Florence, Italy, Sep. 2020, pp. 1–6.

[31] T. Spreng, U. Prechtel, B. Schönlinner, V. Ziegler, A. Meusling, and U. Siart, "UWB near-field MIMO radar: Calibration, measurements and image reconstruction," in *Proc. Eur. Radar Conf.*, Nuremberg, Germany, Oct. 2013, pp. 33–36.

[32] G. Körner, D. Oppelt, J. Adametz, and M. Vossiek, "Novel passive calibration method for fully polarimetric near field MIMO imaging radars," in *Proc. 12th German Microw. Conf. (GeMiC)*, Stuttgart, Germany, Mar. 2019, pp. 150–153.

[33] T. Visentin, J. Hasch, and T. Zwick, "Calibration of a fully polarimetric 8×8 MIMO fmcw radar system at 77 Ghz," in *Proc. 11th Eur. Conf. Antennas Propag. (EUCAP)*, Paris, France, Mar. 2017, pp. 2530–2534.

[34] J. G. Tang, "Polarimetric active radar calibration in target RCS measurement," M.S. thesis, Dept. Elect. Eng., Beihang Univ., Beijing, China, 2016.

[35] T. Liu, X. He, and X. Xu, "Comprehensive characterization of an ellipsoidal cylinder calibrator for radar cross section measurement," *IEEE Trans. Antennas Propag.*, vol. 70, no. 9, pp. 8400–8414, Sep. 2022, doi: 10.1109/TAP.2022.3168737.

[36] FEKO. (2014). *EM Software & Systems-SA*. Stellenbosch, (South) Africa. Accessed: Feb. 27, 2015. [Online]. Available: http://www.feko.info

[37] X. He and X. Xu, "Physics-based prediction of atmospheric transfer characteristics at terahertz frequencies," *IEEE Trans. Antennas Propag.*, vol. 67, no. 4, pp. 2136–2141, Apr. 2019.

[38] H. A. Wheeler, "The interpretation of amplitude and phase distortion in terms of paired echoes," *Proc. IRE*, vol. 27, no. 6, pp. 359–384, Jun. 1939.

Xiaoyu He was born in Jiangxi, China, in 1991. He received the B.S. degree from the School of Mechanical and Electric Engineering, Guangzhou University, Guangzhou, China, in 2012, and the Ph.D. degree in signal and information processing from the School of Electronics and Information Engineering, Beihang University, Beijing, China, in 2018.

He is currently a Lecturer with the School of Electronics and Information Engineering, Beihang University, where he was mainly involved in research of characteristic modeling for multispectral and hyperspectral imagery, radar system modeling, and signal processing.

Tianjin Liu was born in Shandong, China, in 1996. He received the B.S. degree from the School of Information Science and Technology, Dalian Maritime University, Liaoning, China, in 2019. He is currently pursuing the Ph.D. degree in signal and information processing with the School of Electronics and Information Engineering, Beihang University, Beijing, China.

His research interests include radar cross section (RCS) measurement, polarimetric calibration, and radar imaging.

Jingzhe Shan was born in Shaanxi, China, in 1996. He received the B.S. and M.S. degrees from Beihang University, Beijing, China, in 2018 and 2021, respectively, where he is pursuing the Ph.D. degree.

His research interests include asymptotic computational electromagnetics and synthetic aperture radar (SAR)/ISAR imaging.

Xiaojian Xu (Member, IEEE) was born in Jiangxi, China, in 1963. He received the B.S. degree in electrical engineering from the Hefei University of Technology, Hefei, China, in 1983, the M.S. degree in electrical engineering from the Beijing Institute of Environmental Features (BIEF), Beijing, China, in 1986, and the Ph.D. degree in electrical engineering from the University of Nebraska–Lincoln, Lincoln, NE, USA, in 2002.

From 1986 to 1999, he was with BIEF, where he was mainly involved in research of electromagnetic scattering modeling and microwave imaging. From June 1999 to December 2002, he was with the Environmental Remote Sensing Laboratory, University of Nebraska–Lincoln, where his research work was on ultrawideband random noise radar with emphasis on foliage and ground penetration applications. Since January 2003, he has been with the School of Electronic and Information Engineering, Beihang University, Beijing, as a Signal and Information Processing Professor. His research interests include remote sensing signatures, radar imagery, target recognition, and system modeling.